



## Thermal stability analysis of cylindrical thin-walled tanks subjected to lateral fire loading

A. Pourkeramat<sup>1</sup>, A. Daneshmehr<sup>1\*</sup>, K. Aminfar<sup>1</sup>, S. Jalili<sup>2</sup>

<sup>1</sup> School of Mechanical Engineering, University of Tehran, Tehran, Iran

<sup>2</sup> Faculty of Mechanical Engineering, Sahand University of Technology, Tabriz, Iran

**ABSTRACT:** Thin-walled cylinders are widely used as fluid storage tanks, such as water, which is a vital component in extinguishing facilities. Due to the thinness essence of these structures, the stability performance will be put in peril when exposed to various destabilizing side loads. Lateral thermal loads resulting from side fires can lead to unstable behavior of the tanks. The combustion and fire formation are multi-physics phenomena and require a multi-phase fluid perspective to analyze them more closely. In this study, to enhance the analysis's accuracy, the large eddy simulation approach is used to model the fire and estimate its thermal effects on the adjacent structures. The results are consequently utilized for nonlinear stability analysis. The fire simulation results for empty and half-filled tanks are exploited to study the influence of various structural parameters such as geometrical imperfection, roof thickness, and the shell thickness distribution on the critical buckling temperature and instability time. The results reveal that the structure's lateral thermal stability will be maximized at a specific ratio of the roof to the wall thickness. The stepped shell profile, as well as the geometrical imperfection of each configuration, can reduce the critical threshold by up to 40% and weaken the structure against heat. The present research outcomes would help the structural optimizing process of a fire-extinguishing tank subjected to fire-induced instability.

### Review History:

Received: Mar. 31, 2020

Revised: Jul. 05, 2020

Accepted: Oct. 25, 2020

Available Online: Nov. 02, 2020

### Keywords:

Fire

Thermal buckling

Storage tanks

Numerical methods

Large eddy simulation

### 1- Introduction

Storage tanks are abundantly found in various shapes and types for keeping fluids in multiple industries. Water storage tanks are among the most important containers used in urban water supply networks, factories, and fire stations. Studying and evaluating the destruction of such containers is essential to increase safety and efficiency.

The nature of thin-walled structures makes them highly susceptible to destabilizing loads. Among the most critical factors causing catastrophic incidents, heat and its heterogeneous distribution in thin shells often lead to irreparable damages. Instability frequently occurs in the form of buckling in the tanks, which could be due to the emergence of compressive stresses in the structure because of thermal loading. Structures exposed to high temperatures, which in most cases have no uniform distribution, tend to expand significantly, which induces compressive circumferential membrane stresses. This high induced heat for a structurally constrained shell commences a change in the axial membrane force around the shell's perimeter and the critical value of the axial thermal stress distribution. The critical buckling time and temperature calculation are firmly dependent on the temperature pattern and should be sufficiently performed. Even if the temperature gradients are small, it can lead to

buckling in the structure, and eventually, the structure may collapse [1-4]. Therefore, accurate detection and investigation of the temperature distribution have an essential role in the favorable prediction of structures' critical load and buckling behavior under different thermal loading conditions.

Regarding that, Godoy and Batista-Abreu [5, 6] have investigated the Bayamon Puerto Rico fire incident in which 21 fluid storage tanks were destroyed due to an adjacent fire. Liu [7] has comprehensively analyzed the analytical and numerical solution for the buckling problem of storage tanks in the vicinity of the fire. In this study, fire is simulated using the solid flame model at different distances and heights, and a half-cosine equation for temperature distribution around the target tank has been presented. On the other hand, buckling and post-buckling of thin-walled cylindrical tanks subjected to different temperature distributions were studied by distinct methods such as Linear Buckling Analysis (LBA), Geometrically Nonlinear Analysis (GNA), Geometrically and Materially Nonlinear Analysis (GMNA), and Geometrically Nonlinear Imperfection Analysis (GNIA). Landucci et al. [8], Goula et al. [9], and Pantousa [10] have investigated the effect of varied fire scenarios on tank failure. Da Silva Santos et al. [11] simulated the fire incidents using the Finite Element Method (FEM) in Abaqus and evaluated the optimal distance for storage tanks' locations.

Furthermore, Pantousa et al. [12] studied the

\*Corresponding author's email: daneshmehr@ut.ac.ir



reinforcements' effect on the structure by using the half-cosine equation and also employed the GNA method to examine the tank's different dimensions, the impact of damping ratio, and roof-wall thickness ratio. Maraveas [13] investigated the effect of fluid level and heating range on the buckling of a cylindrical shell. Moreover, Pourkeramat et al. [14, 15] studied the effect of geometrical imperfection and reinforcement type on an empty and half-filled container using Abaqus and concluded that the horizontal reinforcements would have a better performance in comparison to vertical reinforcements. Jujuly et al. [16] and Espinosa et al. [17] have investigated the fire heat flux received by the target tanks. Fire modeling has been carried out based on the flame pulse and solid flame model around the target container, and its effects on tank failure under several geometrical conditions have been studied [18-20].

Depending on the tank's size and the definition of the problem, it would be very costly or even impracticable to do experimental work in this area. The fire simulation is very elaborate because of the turbulent and transient nature of the flame, as well as the environmental conditions and involvement of multiple parameters. Several semi-empirical and numerical models have been proposed to determine flame behavior. The Finite Volume Method (FVM) through the Large Eddy Simulation (LES) is a well-suited numerical method to simulate fire and combustion processes and predicting its behavior. An advanced open-source LES code is offered by the National Institute of Standard and Technology (NIST-USA), which has been implemented in several creditable studies to simulate fire and its consequences under different scenarios [21, 22]. The proposed code is called Fire Dynamic Simulator (FDS).

For the first time in the present research, the simulation of a fire-pool next to the target tank is investigated adopting the CFD approach, considering the fire's effective heat flux distribution. The time-dependent temperature distribution on the shell is calculated knowing the distribution of heat flux on the container, and nonlinear structural stability analysis is performed. Several structural parameters, such as roof-to-shell thickness ratio, non-uniform lateral wall thickness distribution, as well as the effect of geometrical imperfections on the above parameters, are considered in the analysis of a nonlinear structure. It is expectable that the storage tanks are not always in full capacity service, and in this paper, the effect of half-filled-ness combined with the mentioned parameters also is examined. To the best knowledge of authors, no notable research has been published regarding the response of a half-filled tank subjected to fire loading. The main characteristics of thermal instability, such as the maximum temperature at the onset of buckling, the dominant buckling mode, and the critical time of instability, are analyzed and discussed accordingly.

## 2- Numerical Modeling Procedure

### 2- 1- Fire induced thermal loading

#### 2- 1- 1- Fire and combustion process

The LES method is employed in FDS code to model

combustion, in which the reaction of fuel and oxygen is extremely fast and is only controlled by mixing. In the FDS code, primary species are included in three categories: fuel reaction, air, and products, which are called compact species. Therefore, the reaction equation is considered as Eq. (1), in which the primary species are classified based on the volumetric fraction of the compressed species. The stoichiometric coefficients of the compressed species are obtained from the sum of the stoichiometric coefficients of the primary species [23].



In the majority of FDS applications, since most of the chemical reactions are very fast, the premise that the mixture burns is sufficient to model the reaction system, and the average chemical source term for fuel using the Eddy Dissipation Concept (EDC) is derived by Eq. (2) [23].

$$\dot{m}_F''' = -\rho \frac{\min(Z_F, Z_A / s)}{\tau_{mix}} \quad (2)$$

In which,  $Z_F$  and  $Z_A$  are the mass fraction of compressed fuel and air species, respectively. The stoichiometric coefficient of air mass is denoted as  $s$  and  $\tau_{mix}$  is the time scale for mixing, which has to be modeled. The heat released per unit volume is obtained as a sum of the mass production rates of the species multiplied by the enthalpy of formation as Eq. (3) [23]. In which,  $\dot{m}_\alpha'''$  is mass production rate, and  $\Delta h_{f,\alpha}$  is related to the standard heat of formation of compound  $\alpha$ .

$$\dot{q}''' = -\sum_{\alpha} \dot{m}_\alpha''' \Delta h_{f,\alpha} \quad (3)$$

The radiative transfer equation in the FDS code is solved for gray gas. For the environment, which includes absorption, emitting, and scattering, it can be written as Eq. (4) [23].

$$\begin{aligned} S \cdot \nabla I_\lambda(x, s) = & -\kappa(x, \lambda) I_\lambda(x, s) \\ & -\sigma_s(x, \lambda) I_\lambda(x, s) + B(x, \lambda) \\ & + \frac{\sigma_s(x, \lambda)}{4\pi} \int_{4\pi} \phi(s', s) I_\lambda(x, s') ds' \end{aligned} \quad (4)$$

where  $I_\lambda(x, s)$  is the radiation intensity in the wavelength  $\lambda$ , and  $S$  is the vector for the radiation intensity. The local coefficients of absorption and scattering are shown as  $\kappa(x, \lambda)$  and  $\sigma_s(x, \lambda)$ , respectively.  $B(x, \lambda)$  is the

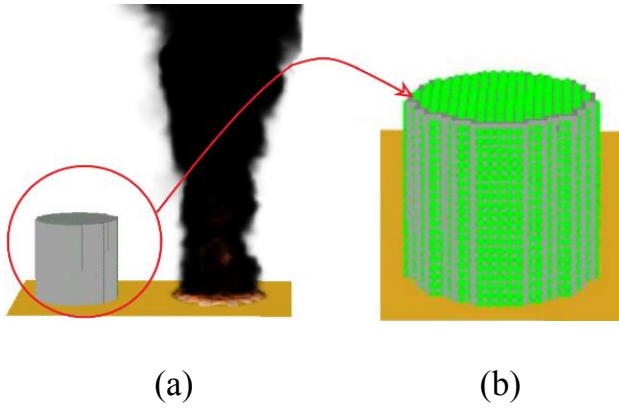


**Fig. 1. (a) General condition of the tank and fire in the FDS code; (b) Zooming in on the target tank to represent sensors (green dots)**

source of radiant energy emission and is equal to the amount of heat released by the local gas mixture, soot, and droplets/particles. The integral term on the right side of the equation represents scattered radiant energy in other directions. By default, FDS solves the radiation transfer equation using 100 discrete angles.

**2- 1- 2- Fire simulation and governing equations**

For analyzing the fire pool effect, which is located in the container’s vicinity, it is assumed that the circular pool’s diameter is 20 m, and its outer surface is located 15 m away from the nearest point of the tank. Experimental studies indicate that by increasing the fire pool diameter, the Heat Release Rate Per Unit Area (HRRPUA) will approach asymptotically to a constant magnitude [24]. In this research, HRRPUA is considered 2400 kW/m<sup>2</sup>, and 10% of total combustion products are set to be soot yield. Fig. 1 (a) illustrates the general arrangement of fire and tank locations. A total of 1149 sensing gages are defined on the target tank’s surface to perceive and quantify the heat flux pattern of fire-induced thermal loading (Fig. 1 (b)). Each gauge continuously records the thermal flux.

The FDS code focuses on smoke and heat transfer in fire incidents. Factors such as turbulent mixing of gas fuel and combustion products with surrounding air are duly considered. The accurate calculation of fluid dynamic equations is dependent on making the gas vertex of mixing big enough. The general solution procedure in NIST proposed code (FDS) consists of low-speed, heat-driven flow Navier-Stoke equations to be solved explicitly using numerical methods with quadratic accuracy order. Although if the grid is sufficiently small, Direct Numerical Simulation (DNS) can be applied, LES is used by default for implementing turbulences in the model. LES approach divides the building space into multiple small grids, solves every conservation equation by

a numerical method, and can accurately anticipate physical data of fire such as fire pressure, temperature, speed, and flow of smoke. Large Eddy Simulation of the fundamental equation of fire dynamics is the simplified low Mach number flow equation. LES approach proves to reduce computational costs and provide more accurate results in comparison with just getting the average of the flow field but not reflecting chronological characteristics of flow. Generally, a fire simulation requires a continuum fluid dynamics approach in which the fundamental continuity, momentum, energy balance, and chemical-mechanical state equations must be satisfied. These primary equations can be summarized as follows [23, 25]:

- Continuity

$$\frac{\partial \rho}{\partial t} + \nabla \cdot \rho \vec{V} = 0 \tag{5}$$

- Momentum conservation

$$\rho \frac{\partial \vec{V}}{\partial t} + (\vec{V} \cdot \nabla) \vec{V} + \nabla p - \rho g - f - \nabla \cdot \tau = 0 \tag{6}$$

- Energy conservation

$$\frac{\partial}{\partial t} (\rho h) + \nabla \cdot \rho h \vec{u} - \frac{F_p}{F_t} - q - \nabla \cdot K \nabla T - \nabla \cdot \sum_i \rho h_i F_i \nabla Y_i + \nabla q_r = 0 \tag{7}$$

- Mass conservation

$$\frac{\partial}{\partial t} (\rho Y_i) + \nabla \cdot \rho Y_i \vec{V} - \nabla \cdot (\rho F_i \nabla Y_i) - W_i = 0 \tag{8}$$

- Gas state

$$P_0(t) - vTR - \sum_i \frac{Y_i}{M_i} = 0 \tag{9}$$

where  $P$ ,  $V$ ,  $T$ ,  $Y$ ,  $\rho$ , and  $h$  are pressure, velocity, temperature, mass concentration, density, and total enthalpy of the flow field, respectively. In addition,  $u$  and  $h$  denote the internal energy and enthalpy, respectively, and diffusion coefficient, Moore molecular weight, and universal gas constant are taken as  $F$ ,  $M$ , and  $R$ , named in the order. Thermal conductivity is mentioned as  $K$ , and  $W$  refers

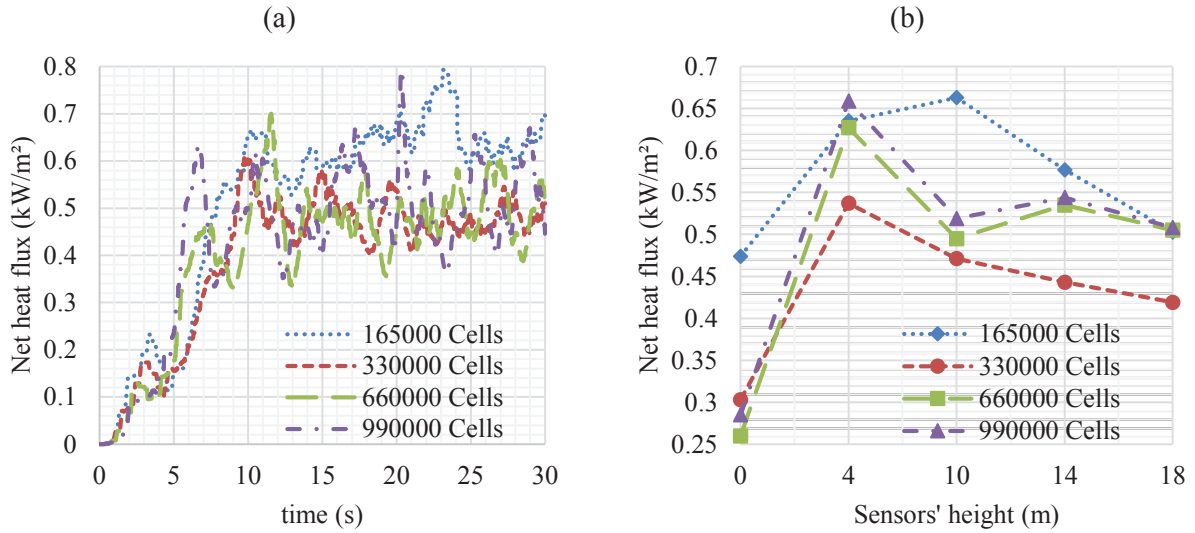


**Fig. 2. Average heat flux received by (a) the sensor within 10 (m) from the ground considering different mesh size; (b) sensors defined at different heights for various cell size**

to chemical reaction speed. Both  $q$  and  $q_r$  introduce heat release attributes in which the latter is associated with the radiation part of the heat. It should be noted that in Eqs. (5) to (9)  $i$  specifies the component in the related term and  $t$  characterizes turbulence.

The described FDS code utilizes the finite volume method to solve governing equations (Eqs. (5) to (9)) and anticipates fire and surrounding behavior. The filter width ( $\Delta$ ) exploited in the LES method is defined in accordance with the cubic root of the cell volume ( $V_c$ ), as indicated in Eq. (10) [23]. In this equation,  $x$ ,  $y$ , and  $z$  are coordinate system components.

$$\Delta = V_c^{1/3} = (\delta x \delta y \delta z)^{1/3} \quad (10)$$

Since the filters in LES are capable of being used for space and time fields, for each continuous field ( $\phi$ ), the filtered field is defined as Eq. (11), in which  $t$  corresponds to time [23].

$$\bar{\phi}(x, y, z, t) \equiv \frac{1}{\Delta^3} \int_{x-\delta x/2}^{x+\delta x/2} \int_{y-\delta y/2}^{y+\delta y/2} \int_{z-\delta z/2}^{z+\delta z/2} \phi(x', y', z', t) dx' dy' dz' \quad (11)$$

A numerical convergence study in LES simulations is conducted by discretizing the surrounding atmosphere by

cubical cells with 40x75x110 m dimensions. All the control volume's outer surfaces are considered to have open boundary conditions except the bottom surface, which is ground. Four grid densities were considered to investigate the sensitivity of the results to the grid dimensions. In this case, five thermal sensors at 0, 4, 10, 14, and 18 m from the ground and in the nearest location to the fire pond were considered. Fig. 2 (a) shows the results of the heat flux received by the 10 m sensor from 0 to 30 seconds. It can be observed that after a high rate of escalating transience in the initial portion of flux history, a relatively low fluctuation around an average quantity is formed. Therefore, the average heat flux is measured in a period of 20 to 30 seconds. The total heat flux of sensors at different elevations for each grid is shown in Fig. 2 (b). Grid density study reveals that the mesh with 660000 cells will be the right choice based on both precision and calculation cost, with an average difference of less than 3% from the finest discretization. In this density, there are 75, 40, and 220 cells in longitude, width, and height directions, respectively.

### 2- 2- Structural analysis

The geometrical condition and a typical heat flux distribution pattern in the tank are illustrated in Fig. 3. The structure is modeled in a simply supported condition at the base and has a shallow conical roof with a 10-degree slope ( $\alpha$ ) and a thickness of two times the shell ( $t_2/t_1$ ). The cap is integrated with the lateral shells without considering any contact line characteristics, and the container is recognized as one piece. In other words, the connection type between roof and walls is ignored. The tank's diameter (D) and height (H) are 20 m, and its thickness ( $t_1$ ) is 0.01 m. All parts are

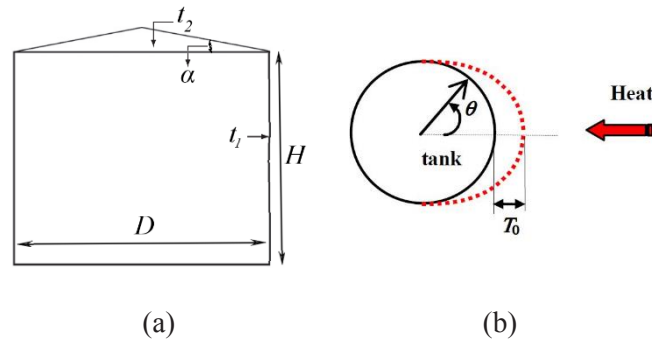


**Fig. 3. (a) The storage tank geometrical parameters; (b) Typical pattern of temperature distribution on the target tank**

**Table 1. Material properties for Steel 275 [1, 5, 26]**

T (°C)	25	100	200	300	400	500	600	1000
Conductivity (W/m <sup>2</sup> K)	53.5	51	47.6	44.2	40.8	37.6	34.0	27.4
Thermal expansion coefficient (1/μ°C)	12.4	13.0	14.1	15.1	16.0	17.0	18.0	22.1
Poisson's ratio	0.288	0.293	0.293	0.294	0.299	0.300	0.306	0.358
Young's modulus (GPa)	210	210	191	169	148	127	66	9.5
Yield strength (MPa)	275	275	275	275	275	215	129	11

**Table 2. The normalized temperature at the onset of instability for different grid intensities.**

Number of elements	12096	19440	29788	32938	41520	62190	67858	77596	79920
$T_{cr}^m$	0.710	0.876	0.948	0.975	0.976	0.990	0.997	0.999	1

influenced by gravity (9.81 m/s<sup>2</sup>).

The structure is made of Steel 275, and its mechanical properties are shown in Table 1. Since the structure's temperature may reach several hundred degrees Celsius, the changes in the material properties become more meaningful with escalating temperatures. Hence differences in material properties such as modulus of elasticity, Poisson's ratio, expansion coefficient, specific heat, conductivity, and plastic properties are considered according to the temperature.

In the present study, the tank's initial temperature and the liquid inside it are considered 25 °C. Water density is assumed to be 997 kg/m<sup>3</sup>. Although the stored liquid temperature will slightly change after a long time, it would be feasible to assume that the temperature variation of stored fluid is negligible during thermal loading and structural stability analysis. The assumption is based on the fact that the volume of water and its thermal capacity is much higher than the metal part of the tank. According to the main context of the present study, which is also in line with other credible published studies [1,5,7], the mass of containing fluid has

no tangible effect on static-Riks analysis due to the absence of dynamic forces and related inertial effects in the static equilibrium of the structure. Therefore in this stage of the research, the fluid inertia's effects ( i.e., mass) are ignored. However, the liquid's hydrostatic pressure is applied to the lateral shells in all of the simulations.

For nonlinear structural stability analysis of the container, the nonlinear arc-length procedure in ABAQUS/Standard environment is implemented [27, 28]. The numerical model of the thin-walled tank was constructed using finite deformation S4R shell elements. The temperature distribution and its temporal evolution were calculated using extracted fire-induced heat flux (from LES code) in ABAQUS/heat transfer by utilizing scripts in Python.

Nine discretization cases were employed and the comparison is depicted in Table 2 for numerical convergence study and determination of optimal mesh. In this table,  $T_{cr}^m$  refers to the normalized maximum temperature in the structure at the instance of instability. Therefore, the case with 67858 elements having 360 and 40 elements along

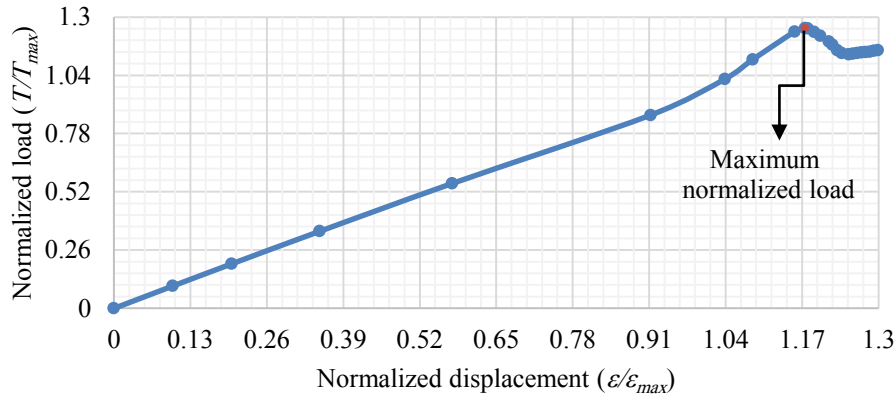


**Fig. 4. LPF diagram in the empty tank**

the circumference and the height directions, respectively, is considered as the optimal grid. The portions of the structure with intense geometrical variations and stress concentration, such as the junction of roof, tank, and ground, are discretized by finer meshes in comparison to global seeding.

**2- 2- 1- Nonlinear structural stability analysis**

In most cases, when structures are subjected to high loads, large deformations follow nonlinear equations. Nonlinear buckling analysis could be obtained by exploiting the arc-length (Riks) method. By increasing the loading until forcing the structure into an unstable condition, the arc-length method could anticipate the next step’s equilibrium. Each increment is applied based on a specific amplification in loading values, as proposed in Eq. (12). In this equation,  $P_0$  is the initial load,  $P_{ref}$  is the reference load vector, and  $\lambda$  is the load proportionality factor, which is derived at each increment and is used in the next steps [28].

$$P_{total} = P_0 + \lambda(P_{ref} + P_0) \tag{12}$$

The Riks method uses the Newton method for solving the nonlinear equilibrium equations with an extrapolation with a 1% strain increase. Considering the static equilibrium path, an initial amplification in arc length ( $\Delta l_{in}$ ) occurs when the Riks method is exploited. Eq. (13) determines the initial value of the load proportionality factor ( $\Delta \lambda_{in}$ ), where usually the scale of the arc length ( $l_{period}$ ) is assumed to be 1 [28].

$$\Delta l_{in} = \frac{\Delta \lambda_{in}}{l_{period}} \tag{13}$$

The procedure of obtaining the solution for the arc-

length method is to initially use the value of  $\Delta \lambda_{in}$  for the first iteration to determine  $\lambda$ , and then it is calculated automatically.

One of the arc-length method’s main applications is in nonlinear stability analysis, which is conducted by interpreting the Load Proportionality Factor (LPF) diagram. For example, Fig. 4 shows the variation of proportionality factor related to the thermal loading (i.e., temperature imposed on the structure) in the empty tank case. In this graph, which is created for a geometrically perfect tank, the amplitude of imposed temperature in the arc-length analysis is chosen to be 142 °C. Although there is no obligation to select a specific temperature, this magnitude is the maximum temperature observed in transient heat transfer analysis after 50 minutes of simulation. The load factor in which a sudden change in the curve’s slope is observed could be considered as the onset of nonlinear buckling load (temperature) of the structure. In this diagram, the value of 1.25 of normalized load denotes  $1.25 \times 142 \text{ °C} = 177.5 \text{ °C}$  of thermal buckling temperature. This shows that the required temperature for instability was higher than the initially applied temperature in the arc-length analysis. In some cases (such as imperfect structures, which will be discussed in subsequent parts), it is quite possible that lower temperatures (less than 142 °C) lead to thermal instability.

**3- Verification of the Numerical Procedure**

**3- 1- Verification of fire and combustion simulations**

Experimental research by Fleury [29] has been used to verify the LES outcome. In that research, the amount of heat flux received by the gages from a rectangular 0.6x0.4 m<sup>2</sup> fire-pool has been investigated. The fuel was Propane with a Heat Release Rate (HRR) of 300 kW. In the present study, the experiment reported in reference [29] has been simulated in the open-source fluid code, carefully positioning several sensors at different distances and directions, as can be seen in Fig. 5. The net heat flux value for each sensor at a particular time is calculated and illustrated in Fig. 6. Perceptibly, with

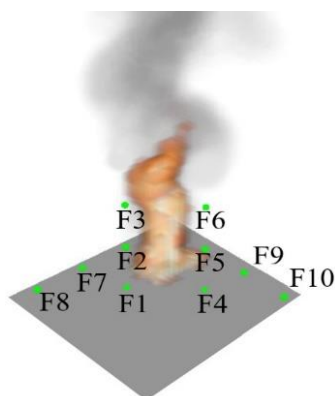


Fig. 5. Sensors locations

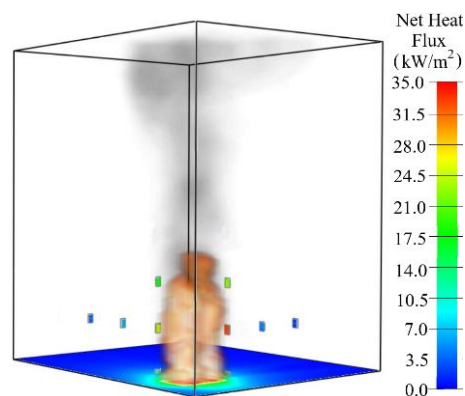


Fig. 6. The amount of heat flux received by the bottom zone and the sensors at 30 seconds after starting the fire

Table 3. Heat flux received by each of the gages and their location in the reference test [29]; Z and L are height from the ground and distance from the fire center, respectively

Sensor name and location	Z (cm)	L (cm)	Numerically calculated average heat flux (kW/m <sup>2</sup> )	Experimentally measured average heat flux [29] (kW/m <sup>2</sup> )
F1-side	0	50	11.082	14.268
F2-side	50	50	21.938	21.585
F3-side	100	50	16.018	15.610
F4-front	0	50	9.706	11.463
F5-front	50	50	19.852	18.537
F6-front	100	50	16.072	13.659
F7-side	50	100	5.971	7.318
F8-side	50	150	2.137	3.603
F9-front	50	100	6.528	6.764
F10-front	50	150	2.775	3.494

increasing distance from the center of the fire-pool, the heat flux decreases significantly, and the maximum value occurs close to half the height of the flame due to the increased view factor of the sensor to the fire. Gages' location information and corresponding mean heat flux values obtained in the steady-state analysis are presented in Table 3. Based on the results, the total differences between the LES numerical method and the experiment are within 16% range.

In the present research, thanks to the FDS code, the received thermal flux is recorded at each moment for each of the embedded sensors shown in Fig. 1. This thermal flux is then inserted into Abaqus by Python scripting. Then, through the heat transfer method and employing the DS4 elements (4-node heat-transfer quadrilateral shell elements

[27]), the temperature distribution is obtained according to the tank's geometrical conditions. Fig. 7 (a) shows the heat flux distribution of the target tank and the surrounding environment at 30 seconds after the start of the fire. Since the shape of the flame varies at each moment, the absorbed heat flux in each gauge will not be the same according to the time. For example, Fig. 7 (b) shows the distribution of thermal flux at any given time at altitudes of 0, 4, 8, 12, 16, and 20 m above the ground for sensors located at the closest distance from the fire to the target tank. As can be seen from this figure, the amplitude of the oscillations is almost constant over time. For this purpose, the interval of 20 to 30 seconds after the start of the fire is averaged in each thermal flux sensor so that the constant amount of thermal flux in each sensor enters

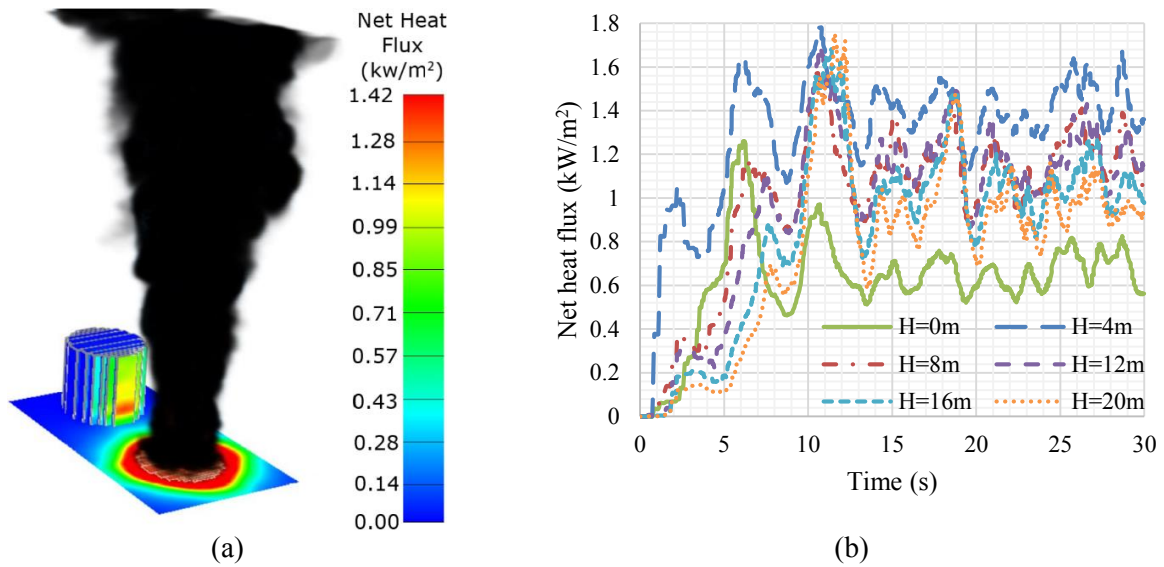


Fig. 7. Heat flux distribution (a) in FDS; (b) for gages located at different heights versus time

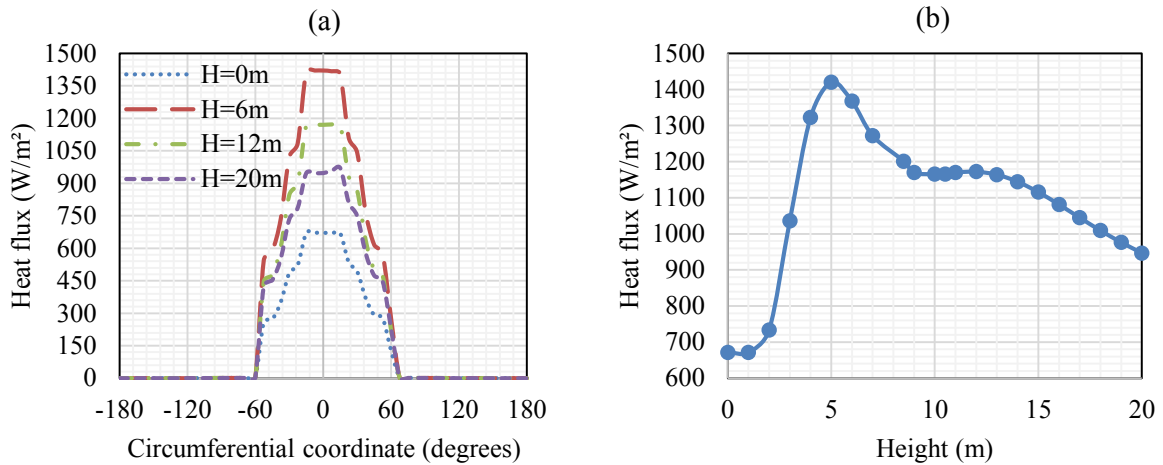


Fig. 8. Heat flux values received by the target tank; (a) peripherally; (b) along with the height (axial direction)

Abaqus.

Fig. 8 illustrates the heat flux magnitude reported on different sensors along the perimeter and axial (i.e., height) directions. Fig. 8 (a) shows that the maximum heat flux distributions are obtained at the closest distance to the fire-pool along the peripheral direction for various heights. Heat flux variation along the height direction on the closest line to the fire pool is depicted in Fig. 8 (b). It is observable that in this direction, the maximum heat flux occurs at 5 m height, which has the maximum fire view onto the fire flames. After 5 m of height, the heat flux is deteriorated due to smoke and reduced fire view factor.

Fig. 9 shows the temperature distribution at the onset of buckling for the empty and half-filled tanks due to the thermal flux of Fig. 7 (a), where the shell has uniformly 1 cm, and the ceiling has 2 cm thickness. In the half-filled tank, a noticeable temperature difference is not detected in the lower water-filled part because of the water's ability to absorb and transfer the heat.

### 3- 2- Verification of nonlinear structural instability analysis

Reference [5] results are used in this section to examine the performance of the proposed nonlinear stability analysis. Referring to Fig. 3 (b), the temperature distribution around

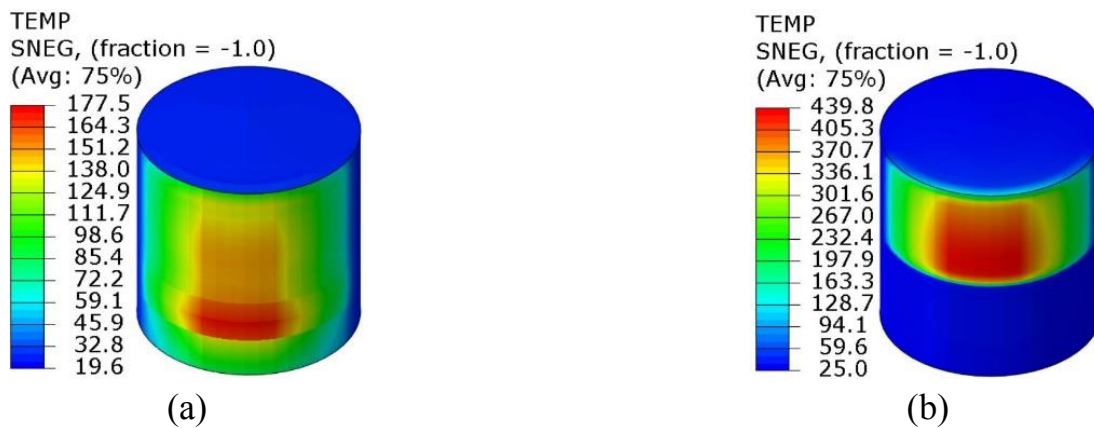


Fig. 9. Temperature distribution in (a) empty tank; (b) half-filled tank

Table 4. The critical buckling temperature comparison

$\theta_0$	Reference [5]	Arc-length procedure	Difference (%)
67.5°	118	116.5	1.27
90°	128	126	1.56
112.5°	146	147.3	0.89
135°	220	226	2.65

the target object is presented as follows:

$$T_\theta = \begin{cases} (T_{0m} - T_{0a}) \cos^2\left(\frac{\theta}{\theta_0}\right) & \text{if } |\theta| \leq \theta_0 \\ 0 & \text{if } |\theta| > \theta_0 \end{cases} \quad (14)$$

In which  $\theta$ ,  $T_{0m}$ , and  $T_{0a}$ , are the circumferential coordinate, the temperature at the most heated altitude of the tank in (°C), and ambient temperature in (°C), respectively. The critical angle which defines the heated zone,  $\theta_0$ , was assumed to have different values such as 67.5, 90, 112.5, and 135 degree.

In reference [5],  $t_1$  and  $t_2$  are 6.35 mm and 12.70 mm, H and D are 12.20 m and 14.64 m, respectively, and  $\alpha$  is considered as 0.1875 degree. The critical buckling temperature obtained by the arc-length method is shown in Table 4. Based on the results, the numerical method used in this study would have less than 3% differences for every critical degree ( $\theta_0$ ) comparing with the reference [5], confirming that the present numerical procedure is reliable enough for subsequent analysis.

#### 4- Results and Discussion

##### 4- 1- Geometrical imperfection's effect

Geometrical imperfections are an inevitable feature of structures that often result in vulnerability and premature collapse due to destabilizing loads. Such deviations from ideal geometrical configurations often happen in the construction process of structures, and even the most accurate manufacturing methods are associated with defects.

One of the accepted procedures to apply the imperfections on the thin wall structures is based on the weighted combination of the Eigen-valued modal response of the structure, such as linear buckling or Eigen-frequency analysis [28]. By increasing the Eigen-mode number, it is anticipated that the mode contribution to the imperfection will decrease. In this study, the first, second, and third modes of linear buckling analysis with the normalized ratios of 1, 1/10, and 1/100 of the imperfection amplitude, respectively, have been imported into the model. The buckling mode shapes are multiplied by 0%, 10%, 20%, 40%, 60%, 80%, 100%, 200%, and 400% of the shell thickness to investigate the effect of imperfection intensity.

Fig. 10 shows the LPF curve in different geometrical imperfections thresholds. This figure shows that as the geometrical imperfection amplitude increases, the normalized

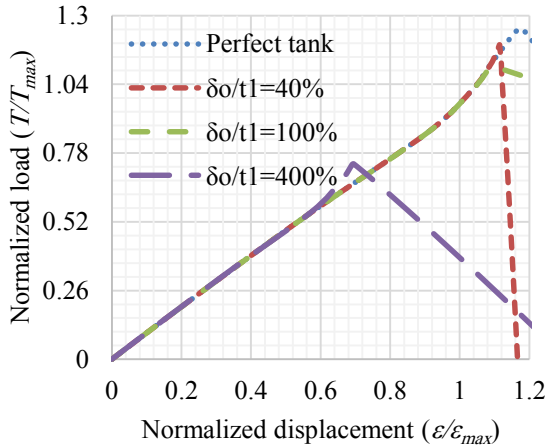


**Fig. 10. LPF diagram for different imperfection intensities**

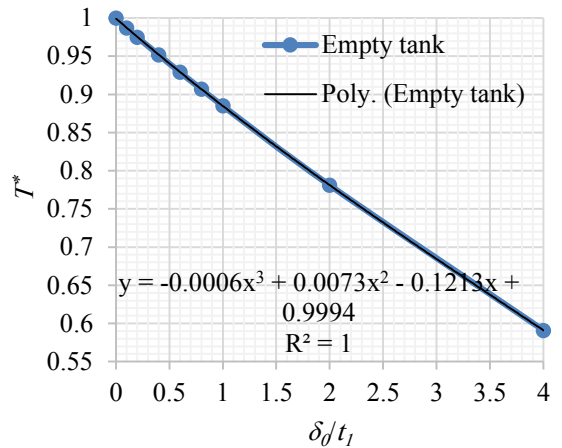


**Fig. 11. Effect of geometrical imperfection on the critical buckling temperature in the empty tank**

load value diminishes, indicating that the critical temperature declines.

The dimensionless buckling temperature ( $T^*$ ) for the empty storage tank with increasing geometrical imperfection amplitude ( $\delta_0$ ) is presented in Fig. 11. In this case,  $T^*$  is defined as the ratio of critical buckling temperature for the imperfect ( $T_{cr}$ ) to the perfect structure. The perfect tank's critical buckling temperature was calculated as 177.5 °C. As can be seen in Fig. 11, by increasing the imperfection intensity, more than 40% of perfect structure stability capacity could be lost. A third-order polynomial could be fitted to obtain a  $T^*$  estimation relation as a function of imperfection amplitude for the empty tank case (Eq. (15)).

$$\frac{T_{cr}}{T_{cr\_perfect}} = -0.0006\left(\frac{\delta_0}{t_1}\right)^3 + 0.0073\left(\frac{\delta_0}{t_1}\right)^2 - 0.1213\left(\frac{\delta_0}{t_1}\right) + 0.9994 \quad (15)$$

Studies on the half-filled tanks reveal the negligible effect of imperfection amplitude on the stability threshold of structures. Therefore, it could be argued that the detrimental effect of geometrical imperfections in the case of filled tanks would be alleviated.

#### 4- 2- The impact of the roof presence

The roof covering is an important section in the structural design of storage tanks. This part's subtle effect on the structure's lateral thermal stability is studied in the present section. The main factor in this survey is the thickness of the conical roof shell. Therefore, thicknesses of 1, 2, 5, 10, 50, and 100 cm were considered to determine the effect of

roof thickness. A thicker roof means more axial preloads on the lateral shell of the tank. Moreover, as the roof thickness increases, the rate of heat propagation in this part of the structure will decrease, and naturally, a higher temperature gradient between the roof and the lateral shell is formed. Fig. 12 illustrates the difference between the roof's temperature and the body of the tank for different ratios of the roof to body thickness. In this diagram,  $T_1$  and  $T_2$  are maximum body and roof temperatures at the onset of buckling, respectively, in degrees Celsius. Also,  $T_{0a}$  presents the ambient temperature (25 °C), and  $t_2/t_1$  is the thickness ratio of the roof to the walls. In this analysis, the thickness of the shell is constant and equal to 1 cm. This figure shows that as the thickness of the roof increases, its resistance to temperature alteration amplifies, and therefore over time, the roof temperature approaches the ambient temperature.

Fig. 13 shows the buckling mode shapes in the empty and half-full water storage tank. Consistently, at the lowest roof thickness, a higher thermal impression of a thinner roof leads to more temperature distribution and, therefore, more expansion. A stronger tendency to expand in the thinner roof will induce compressive stress, and therefore instability could be observed in this section. Furthermore, the thinner roof's lighter weight creates much less axial compressive force on the sidewalls, and thereupon the side shell will experience more suitable thermo-mechanical loading conditions. In contrast, as the roof's weight and thickness increase, the thermal distribution in this part of the structure becomes more localized, and a tendency for less expansion in the roof of the tank will be observed. However, faster and broader heat distribution in the side walls leads to a greater desire for radial expansion. Correspondingly, the tank's roof will experience more in-plane tension stress while imposing more axial weight on the tank's walls. Obviously, in such a situation, the tank's lateral part is more prone to instability,

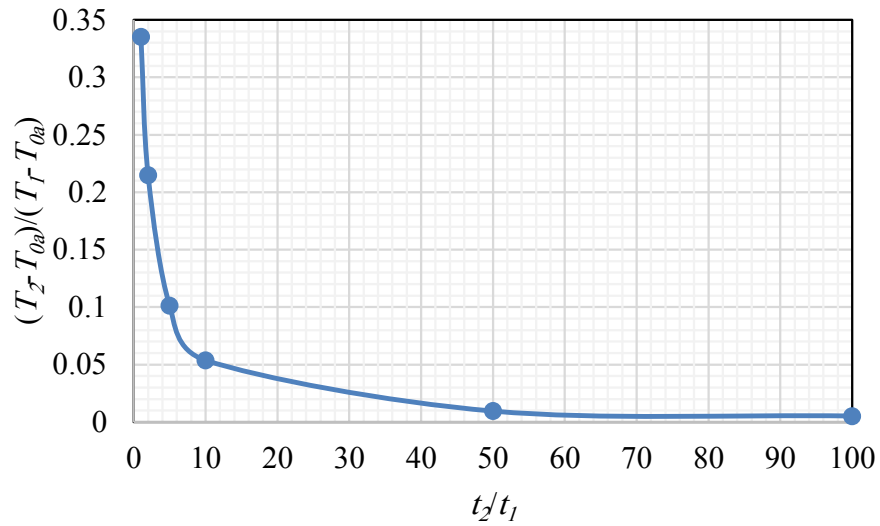


**Fig. 12. Effect of thickness ratio on the temperature difference at the conjunction edge of the roof to the side shell**

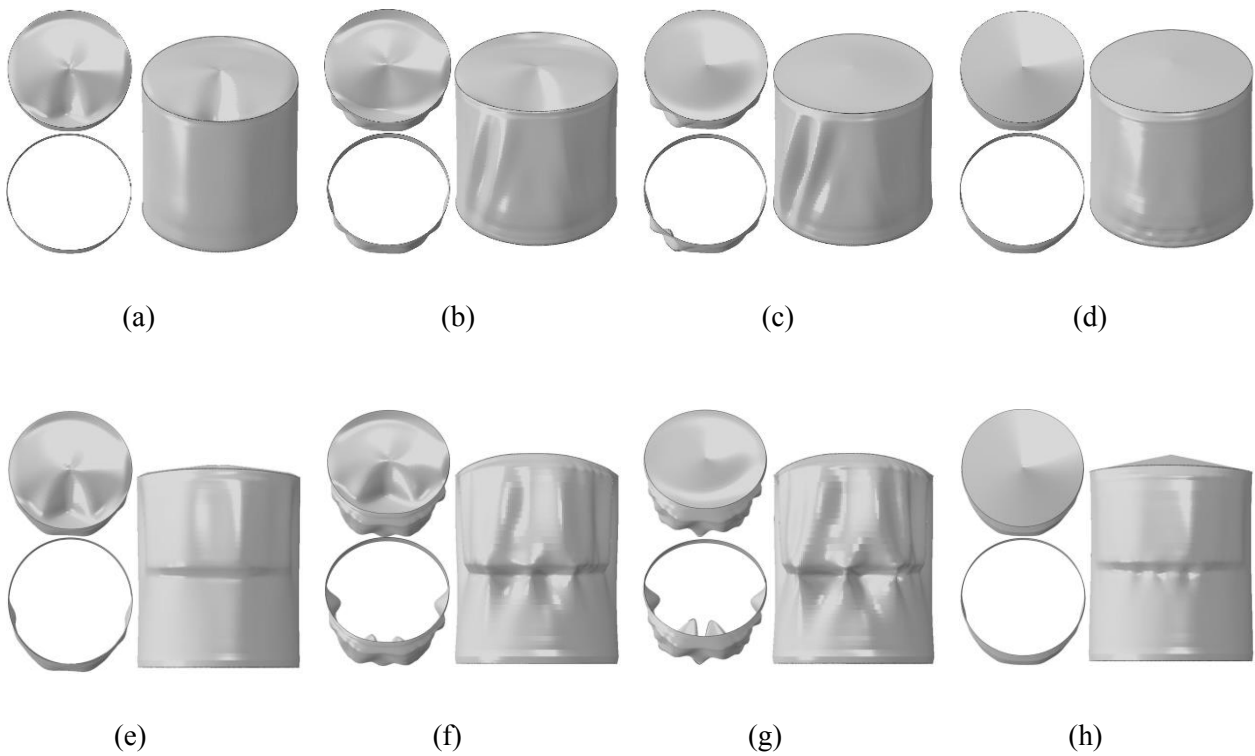


**Fig. 13. The influence of roof thickness on buckling mode shapes; (a) 1 cm for the empty tank ( $T_{cr} = 79.15 \text{ }^\circ\text{C}$ ); (b) 2 cm for the empty tank ( $T_{cr} = 177.59 \text{ }^\circ\text{C}$ ); (c) 10 cm for the empty tank ( $T_{cr} = 162.38 \text{ }^\circ\text{C}$ ); (d) 100 cm for the empty tank ( $T_{cr} = 144.71 \text{ }^\circ\text{C}$ ); (e) 1 cm for the half-filled tank ( $T_{cr} = 177.36 \text{ }^\circ\text{C}$ ); (f) 2 cm for the half-filled tank ( $T_{cr} = 440.78 \text{ }^\circ\text{C}$ ); (g) 10 cm for the half-filled tank ( $T_{cr} = 456.25 \text{ }^\circ\text{C}$ ); (h) 100 cm for the half-filled tank ( $T_{cr} = 182.82 \text{ }^\circ\text{C}$ )**

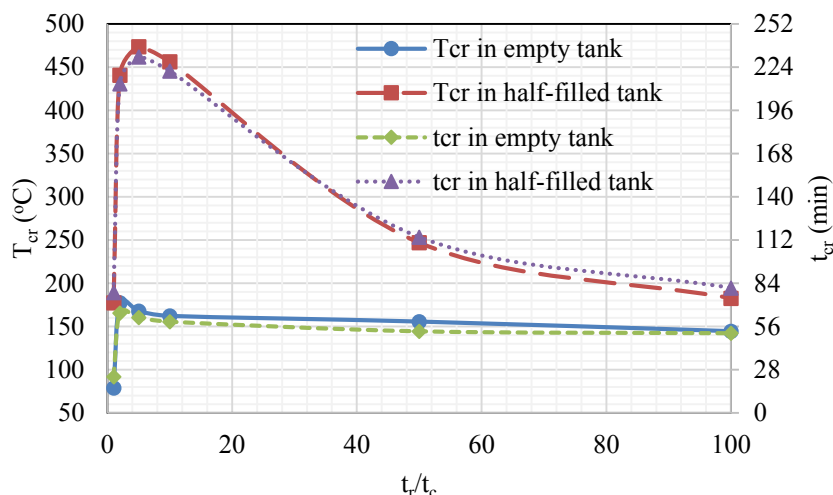


Fig. 14. The influence of the roof thickness on the critical buckling temperature and the time to reach it

Table 5. Dimensions of the tank with a stepped profile

parameter	$H$	$h_1$	$h_2$	$t_a$	$t_b$	$t_c$	$t_d$	$t_e$	$t_f$
quantity (mm)	2000	2020	8100	11.4	10.1	8.8	7.5	6.2	6

and the buckling lobes will be transferred to this portion. The presented study revealed that for the roof with 2 cm thickness, both the roof part and side walls would experience instability.

Fig. 14 illustrates the variation of critical temperature as a function of the roof to side shell thickness ratio. The compressive axial preload applied to the wall's edge can lead to the development of considerable tensile membrane stresses along the peripheral cylindrical section of the container. As a result, more thermal loading will be required to overcome these stresses. The tensile stress positive effect appears as a 124% increase in the critical buckling temperature when changing the roof thickness from 1 to 2 cm. For the half-filled tank case, the optimum thickness will be slightly higher and equals to 5 cm. One of the reasons for the increase in the tanks' permissible axial load is the augmentation of the peripheral membrane tensile stress due to hydrostatic pressure. The growth of the thermal stability threshold of the half-filled tank is 167% when increasing the thickness from 1 to 5 cm.

Further examination of Fig. 14 for the half-filled tank reveals a sharper decrease in critical temperature after passing the optimum range of roof thickness, which is three times more intense in comparison with the empty tank case.

#### 4- 3- Effect of sidewall thickness distribution

Cylindrical thin-walled tanks are often made in stepped wall profile in the interest of their higher cost-effective

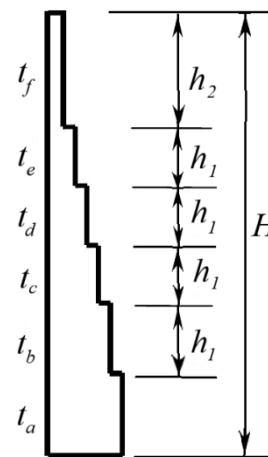
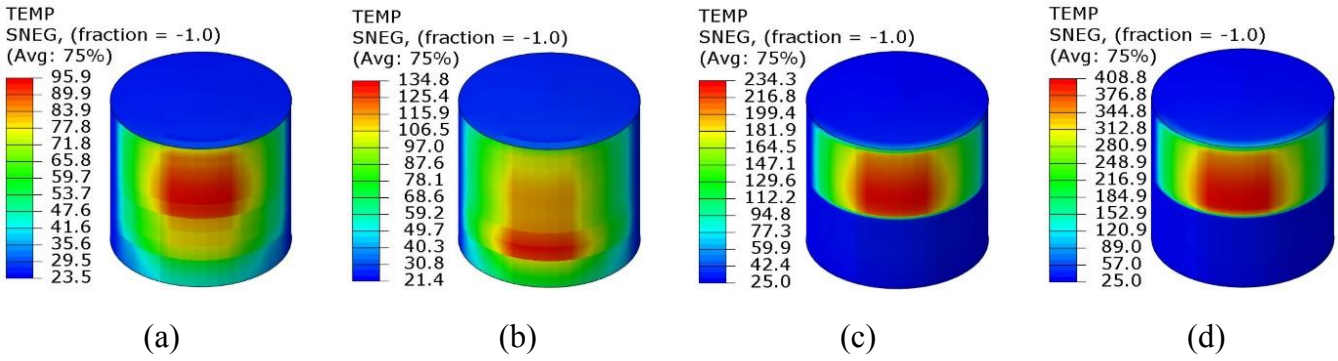
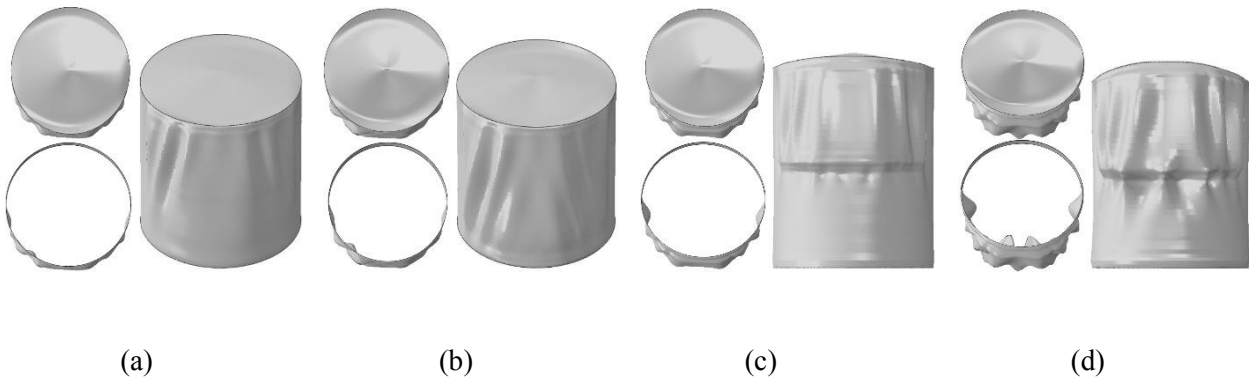


Fig. 15. stepped wall profile

tolerance to hydrostatic fluid pressure. To investigate the structural behavior and resistance of this type of structure to fire incidents, a tank with variable thickness has been considered concerning the proposed construction standards of table A-2a of API 650 [30]. Subscripts in Fig. 15 denote different geometrical attributes for the structures, in which  $t$  is thickness and  $h$  defines height. The dimensions of this tank are visible in Table 5. The average thickness value, in this



**Fig. 16. Temperature distribution at the onset of buckling; (a) stepped-wall empty tank; (b) uniform 7.9 mm thick empty tank; (c) stepped-wall half-filled tank; (d) uniform 7.9 mm thick half-filled tank**



**Fig. 17. Buckling mode shapes; (a) stepped wall empty tank; (b) uniform 7.9 mm thick empty tank; (c) stepped wall half-filled tank; (d) uniform 7.9 mm thick half-filled tank**

case, is 7.9 mm.

Fig. 16 shows the temperature distribution in the empty and half-full tanks for a uniform and stepped wall thickness at the onset of thermal instability. For the uniform thickness, it is observed that maximum temperature occurs in a zone beneath the median height of the tank. In contrast, in the case of stepped thickness, the most affected zone migrates to the upper portion of the storage tank. This returns to the fact that thinner parts of the shell are located in the upper section of the cylindrical storage tanks, and due to lower structural volume, the fire loading leads to a higher temperature in this zone.

The mode shapes for the stepped wall and uniform storages can be seen in Fig. 17. In the stepped wall tanks, heat propagates agilely in the thinner portions and causes rapid expansion, which, due to the resistance to deformation, significant compressive stresses would be developed. Therefore, buckling lobes are observed in the thinner zone, and the critical temperature corresponding to the instability also decreases substantially in comparison to the uniform

wall profile. Table 6 summarizes the critical time ( $t_{cr}$ ) and temperature ( $T_{cr}$ ) corresponding to instability instant of stepped and uniform thickness distribution. Data scrutinizing reveals that thickness stepping would results in a 43% and 29% reduction in stability capacity for half-filled and empty tanks, respectively. It seems necessary to reinforce the thinner zone of the structure with a set of reinforcing elements to prevent large deformations and consequent progressive collapse.

### 5- Conclusions

The heat from adjacent fires could lead to structural instability phenomena in thin-walled fluid storage facilities. In this study, the computational fluid dynamics approach with large eddy simulation is utilized to simulate the lateral fire-pool to predict the thermal loading on the thin-walled empty and half-filled cylindrical tanks more accurately.

The results show that in the empty tanks, geometrical imperfections could lead to a maximum of 41% reduction

**Table 6. The effect of shell thickness variation on the critical buckling temperature and the time to reach it**

Thickness variation	$T_{cr}$ in the empty tank (°C)	$T_{cr}$ in the half-filled tank (°C)	$t_{cr}$ in the empty tank (min)	$t_{cr}$ in the half-filled tank (min)
Stepped thickness	96.46	233.85	22	65
Uniform thickness (7.9 (mm))	135.46	408.60	37	156
Uniform thickness (10 (mm))	177.59	440.78	65	213

in thermo-structural stability of cylindrical storage tanks. Present meticulous investigations revealed that in the half-filled cases, imperfections cause a negligible change in the stability behavior of storage tanks.

The roof thickness of containers affects lateral thermal instability. It is observed that there is an optimum range for roof thicknesses, which leads to an extension of the structure’s stability threshold. The uneven distribution of tank side shell thickness would cause the unstable zone to migrate to the upper part of the tank associating with a considerable reduction in the structure’s thermal stability.

Although most storage tanks are constructed by reinforcing elements, the initial design steps to assess the stability behavior of thin-walled cylindrical tanks require a more sophisticated knowledge about the subtleties of fire loading and its thermo-structural effect on these types of structures. The authors believe that the present survey could provide a framework for the subsequent paces involving more exhaustive design procedures.

**Nomenclature**

$\Delta h_{f\alpha}$	standard heat of formation of compound $\alpha$
$B(x,\lambda)$	Source of radiant energy emission
$D$	Tank's diameter
$F$	Diffusion coefficient
$F$	Heat flux gage
$H$	Tank's height
$h$	Total enthalpy of the flow field
$i$	The component in the related term
$I_\lambda(x,s)$	The radiation intensity in the wavelength $\lambda$
$K$	Thermal conductivity
$L$	Distance from the fire center
$M$	Moore molecular weight
$\dot{m}'''$	Mass production rate
$P$	Pressure of the flow field
$q$	Heat release attributes
$q_r$	Heat release attributes of the radiation part
$R$	Universal gas constant
$s$	The stoichiometric coefficient of air mass
$S$	Vector for the radiation intensity
$T$	Temperature of the flow field
$t$	Characterize turbulence
$T^*$	The dimensionless buckling temperature
$T_{0a}$	Ambient temperature
$T_{0m}$	The temperature at the most heated altitude of the tank

$t_l$	Shell thickness
$T_l$	Maximum body temperature at the onset of buckling
$t_2$	Roof thickness
$T_2$	Maximum roof temperature at the onset of buckling
$T_{cr}$	Critical buckling temperature
$t_{cr}$	Critical buckling time
$T_{cr\_perfect}$	Critical buckling temperature in the perfect tank
$T_{max}$	The initial guess close to the critical temperature
$T_{Cr}^m$	The normalized maximum temperature
$u$	Internal energy
$V$	Velocity of the flow field
$W$	Chemical reaction speed
$Y$	Mass concentration of the flow field
$Z$	Height from the ground
$Z_A$	The mass fraction of compressed air species
$Z_F$	The mass fraction of compressed fuel species
$\alpha$	Slope of roof
$\delta_0$	Geometrical imperfection amplitude
$\theta$	The circumferential coordinate
$\theta_0$	The critical angle which defines the heated zone
$\kappa(x,\lambda)$	The local coefficients of absorption
$\rho$	Density of the flow field
$\sigma_s(x,\lambda)$	The local coefficients of scattering
$\tau_{mix}$	Time scale for mixing

**References**

- [1] D. Pantousa, Numerical simulation of oil steel tank structural behavior under fire conditions, University of Thessaly, Greece, Master Thesis, (2015).
- [2] Y. Li, J. Jiang, H. Bian, Y. Yu, Q. Zhang, Z. Wang, Coupling effects of the fragment impact and adjacent pool-fire on the thermal buckling of a fixed-roof tank, Thin-walled Structures, 144 (2019) 106309.
- [3] L. A. Godoy, Buckling of vertical oil storage steel tanks: Review of static buckling studies, Thin-Walled Structures, 103 (2016) 1-21.
- [4] C. A. Burgos, J. C. Batista-Abreu, H. D. Calabró, R. C. Jaca, L. A. Godoy, Buckling estimates for oil storage tanks : Effect of simplified modeling of the roof and wind girder, Thin-Walled Structures, 91 (2015) 29-37.
- [5] L.A. Godoy, J.C. Batista-Abreu, Buckling of fixed-roof aboveground oil storage tanks under heat induced by an external fire, Thin-walled Structures, 52 (2012) 90-101.
- [6] J.C. Batista-Abreu, L.A. Godoy, Thermal buckling behavior of open cylindrical oil storage tanks under fire,

- Journal of Performance of Constructed Facilities, 27(1), (2013) 89-97.
- [7] Y. Liu, Thermal buckling of metal oil tanks subject to an adjacent fire, University of Edinburgh, UK, PhD Thesis, (2011).
- [8] G. Landucci, G. Gubinelli, G. Antonioni, V. Cozzani, The assessment of the damage probability of storage tanks in domino events triggered by fire, *Accident Analysis & Prevention*, 41(6) (2009) 1206-1215.
- [9] C. Goula, Numerical simulation of pool hydrocarbon fires and their effect on adjacent tanks, University of Thessaly, Greece, Master Thesis, (2017).
- [10] D. Pantousa, Numerical study on thermal buckling of empty thin-walled steel tanks under multiple pool-fire scenarios, *Thin-walled Structures*, 131 (2018) 577-594.
- [11] F. da Silva Santos, A. Landesmann, Thermal performance-based analysis of minimum safe distances between fuel storage tanks exposed to fire, *Fire Safety Journal*, 69 (2014) 57-68.
- [12] D. Pantousa, K. Tzaros, M.A. Kefaki, Thermal buckling behaviour of unstiffened and stiffened fixed-roof tanks under non-uniform heating, *Journal of Constructional Steel Research*, 143 (2018) 162-179.
- [13] C. Maraveas, Thermal buckling analysis of thin-walled steel oil tanks exposed to an adjacent fire, in: 23rd Australian Conference on the Mechanics of Structures and Materials (ACMSM23), Southern Cross University, Byron Bay, Australia, (2014).
- [14] A. Pourkeramat, A. Daneshmehr, S. Jalili, K. Aminfar, Geometrical imperfection's effect on thermal buckling of cylindrical water storage tanks subjected to fire, in: The 28th Annual International Conference of Iranian Society of Mechanical Engineers (ISME2020), Amirkabir University of Technology, Tehran, Iran, (2020).
- [15] A. Pourkeramat, A. Daneshmehr, K. Aminfar, S. Jalili, Effect of fluid level on thermal buckling behavior of different reinforced water storage tanks adjacent to pool fire, in: The Biannual International Conference of Experimental Solid Mechanics (XMECH2020), Iran University of Science and Technology, Tehran, Iran, (2020).
- [16] M.M. Jujuly, A. Rahman, S. Ahmed, F. Khan, LNG pool fire simulation for domino effect analysis, *Reliability Engineering & System Safety*, 143 (2015) 19-29.
- [17] S.N. Espinosa, R.C. Jaca, L.A. Godoy, Thermal and structural analysis of a fuel storage tank under an adjacent pool fire, *Fire Research*, 2(1) (2018) 31-36.
- [18] Y. Li, J. Jiang, Q. Zhang, Y. Yu, Z. Wang, H. Liu, C.M. Shu, Static and dynamic flame model effects on thermal buckling: Fixed-roof tanks adjacent to an ethanol pool-fire, *Process Safety and Environmental Protection*, 127 (2019) 23-35.
- [19] S.N. Espinosa, R.C. Jaca, L.A. Godoy, Thermal effects of fire on a nearby fuel storage tank, *Journal of Loss Prevention in the Process Industries*, 62 (2019) 103990.
- [20] D. Pantousa, L.A. Godoy, On the mechanics of thermal buckling of oil storage tanks, *Thin-walled Structures*, 145 (2019) 106432.
- [21] B. Niknam, H. Madani, H. Salari rad, Determining critical wind velocity during Fire accident in alborz tunnel, *Amirkabir journal of Mechanical engineering*, 44(1) (2012) 47-55.
- [22] S.O. Haghani, E. Barati, Numerical study on the effect of blower location on the maximum temperature and spread of smoke in case of fire inside tunnels, *Amirkabir journal of mechanical Engineering*, 53(1) (2020) 1-3.
- [23] K. McGrattan, S. Hostikka, R. McDermott, J. Floyd, C. Weinschenk, K. Overholt, Fire dynamics simulator technical reference guide volume 1: mathematical model, NIST special publication, 1018(1) (2013) 175.
- [24] M.J. Hurley, D.T. Gottuk, J.R. Hall Jr, K. Harada, E.D. Kuligowski, M. Puchovsky, J.M. Watts Jr, C.J. Wieczorek, SFPE handbook of fire protection engineering, Springer, (2015).
- [25] W. Binbin, Comparative research on FLUENT and FDS's numerical simulation of smoke spread in subway platform fire, *Procedia Engineering*, 26 (2011) 1065-1075.
- [26] Y.C. Wang, Steel and composite structures: behaviour and design for fire safety, CRC Press, London & New York, (2002).
- [27] ABAQUS, User's Manuals, Version 6.4, Hibbitt, Karlsson, and Sorensen Inc., Rhode Island, USA, (2003).
- [28] J.N. Reddy, An introduction to the finite element method, 4<sup>th</sup> edition, McGraw-Hill Education, USA, (2018).
- [29] R. Fleury, Evaluation of thermal radiation models for fire spread between objects, University of Canterbury, New Zealand, Master Thesis, (2010).
- [30] API Standard 650, Welded Steel Tanks for Oil Storage, American Petroleum Institute, Washington DC, USA, (2007).

#### HOW TO CITE THIS ARTICLE

A. Pourkeramat, A. Daneshmehr, K. Aminfar, S. Jalili. Thermal stability analysis of cylindrical thin-walled tanks subjected to lateral fire loading. *AUT J. Mech Eng.*, 5(2) (2021) 265-280.

DOI: [10.22060/ajme.2020.18187.5888](https://doi.org/10.22060/ajme.2020.18187.5888)



